RESEARCH ARTICLE

Satoshi Noguchi · Atsushi Toramaru · Taketo Shimano

Crystallization of microlites and degassing during magma ascent: Constraints on the fluid mechanical behavior of magma during the Tenjo Eruption on Kozu Island, Japan

Abstract Bubble and crystal textures provide information with regard to the kinetics of the vesiculation and crystallization processes. They also provide insights into the fluid mechanical behavior of magma in a conduit. We performed textural (bubble and crystal) and compositional analyses of pyroclasts that were obtained from the Tenjo pyroclastic flow, which resulted on account of the eruption in 838 A.D. on Kozu Island, about 200 km south of Tokyo, Japan. Pyroclasts in one flow unit (300~2,060 kg/m^3; average density 1330 kg/m^3) can be classified into three types on the basis of vesicle textures. Type I pyroclasts have small isolated spherical bubbles with higher vesicularities (67–77 vol.%) and number density (10.8–11.7 log m^{-3}). Type II pyroclasts have vesicularities similar to type I (61–69 vol.%), but most bubbles exhibit evidences of bubble coalescence, and lower number densities than type I (8.9–9.5 log m^{-3}). Type III pyroclasts contain highly deformed bubbles with lower vesicularities (16–34 vol.%) and number densities (8.2–9.0 log m^{-3}). The microlite volume fraction (DRE converted) also changes consistently across type I, type II, and type III as 0.06, 0.08, and 0.10–0.15, respectively. However, the number density of the microlites remains nearly invariant in all the pyroclast types. These facts indicate that the variation in the microlite volume fraction is controlled not by the number density (i.e., nucleation process), but by the size (i.e., growth process); the growth history of each type of microlite was different. Water content determinations show that the three types of pumices have similar H$_2$O contents (2.6±0.2 wt%). This fact implies that all three types were quenched at nearly the same depth (35±5 MPa, assuming that the magma was water-saturated) in the conduit. If the crystal sizes are limited only by growth time, a variation in this parameter can be related to the residence time, which is attributed to the flow heterogeneity in the conduit. By assuming a laminar Poiseuille-type flow, these textural observations can be explained by the difference in ascent velocity and shearing motion across the conduit, which in turn results in the differences in growth times of crystals, degrees of deformation, and bubble coalescence. Consequently, for crystals in the inner part of the conduit, the crystal growth time from nucleation to quenching is shorter than that near the conduit wall. The vesicle texture variation of bubbles in types I, II, and III results from the difference in the deformation history, implying that the effect of degassing occurred primarily towards the conduit wall.

S. Noguchi (✉) · A. Toramaru
Department of Earth and Planetary Sciences, Graduate School of Sciences, Kyushu University,
6-10-1 Hakozaki, Higashi-ku, Fukuoka 812-8581, Japan
e-mail: noguson@geo.kyushu-u.ac.jp
Tel.: +81-92-6422651

T. Shimano
The Center for Northeast Asian Studies, Tohoku University,
Kawauchi, Aoba-ku,
Sendai 980-8576, Japan

Introduction

The fluid mechanical behavior of magma in a volcanic conduit controls not only the intensity of a volcanic eruption but also the eruption style. It is essential to obtain information on fluid mechanics in the conduit during an eruption to understand volcanic eruption mechanisms. Since it is not possible to directly observe the flow of magma in the conduit, it is difficult to quantify characteristics such as velocity and pressure change during magma flow in the conduit. The fluid mechanical behavior of magma in the conduit is influenced by the rheological change in magmas that result from processes including vesiculation, degassing, and microlite crystallization induced by decompression. During dome eruptions, it is reported that the crystallization (Melnik and Sparks 1999) or vesiculation (Wylie et al. 1999) are closely related to the fluid mechanics of magma in the conduit.

Natural products from volcanic eruptions preserve the signature of these complex processes as vesicle and/or microlite textures. In order to infer the dynamics of conduit processes from vesicle and/or microlite textures, the knowledge of the kinetics of vesiculation and crystallization processes is required. Recently conducted experimental studies provide insights into crystallization kinetics under decompression (Geschwind and Rutherford 1995; Blundy and Cashman 2001; Hammer and Rutherford 2002; Couch et al. 2003a, 2003b). The textural analysis of natural products, along with compositional analysis is also a valuable method for understanding the kinetics of nucleation and growth processes in microlite crystallization (Cashman and Marsh 1988; Klug and Cashman 1994; Hammer et al. 1999, 2000; Nakada and Motomura 1999). In addition, some studies (Toramaru 1990; Klug and Cashman 1994; Polacci et al. 2001; Klug et al. 2002) reveal that the vesicle textures in pumice and scoria provide information on the kinetics of the vesiculation process and magma ascent.

Despite these efforts, all the constraints on the fluid mechanical behavior of magma in a conduit are yet to be identified. The constraints on the magma ascent rates for the Mount St. Helens eruption in 1980 using the kinetics of amphibole breakdown (reaction rim formation) are exclusively provided by a study conducted by Rutherford and Hill (1993).

In order to better understand the fluid mechanics of ascending magma including the complex behavior of phase changes, we must address both vesiculation and crystallization processes simultaneously, because a coupling between them through decompression can provide novel constraints on magma ascent processes.

In the present study, we conduct a detailed textural and compositional analysis of pyroclasts from the Tenjo eruption on Kozu Island, Japan. A characteristic feature of some pyroclastic flow deposits of the Tenjo eruption is that they exhibit a wide range of vesicularities. Previous studies report that such a wide range is often observed in a single eruption (e.g., Self and Sparks 1978; Houghton and Wilson 1989). However, the detailed conduit flow processes and the origin of this type of eruption mechanism are not well understood. Therefore, in this paper, we focus on the wide range of vesicularities in the Tenjo pyroclastic products from a single eruption and examine the correlation between the vesicle and microlite textures. Here, we present analytical data and account for the origin of the textural variation using a simple fluid mechanical model of magma ascent in a conduit. First, we will classify the pyroclasts into three types based on vesicle textures. Second, we will present the results of quantitative textural and compositional analyses. Third, we will present a novel correlation between bubble number density and vesicularity. Finally, we discuss the origin of the correlation and the variety of vesicle and microlite textures together with the timing of vesiculation, degassing, and microlite crystallization process, proposing a conduit flow model based on these observations.

Geological outline

Kozu Island

Kozu Island is a volcanic island of the Quaternary age and is part of the Izu-Mariana Island arc about 200 km south of Tokyo (Fig. 1). The island is gourd-shaped, measuring about 6×4 km in size, with a maximum altitude of 574 m a.s.l. The geology of Kozu Island has been reported by Tsuya (1929), Taniguchi (1977), Isshiki (1982), and Suga et al. (1992). There are more than 18 monogenetic rhyolite volcanoes on the island. Eighteen lava domes with similar compositions (76 ± 2.0 wt% of SiO_2, Tsuya 1929) are found in the region. The pyroclastic deposits from these centers exhibit similar lithofacies, which makes the identification of a source dome for each deposit difficult.

The Tenjo lava dome, with a diameter of 1.5 km in north–south, 1 km in east–west and an altitude of 574 m is located in the central region of Kozu Island (Fig. 1). It is a biotite-rhyolitic monogenetic volcano, which last erupted in 838 A.D.

The geology of the Tenjo area is well documented (Taniguchi 1977; Isshiki 1982; Togashi 1984; Ito 1990). The early stages of the Tenjo eruption were phreatomagmatic in nature (Ito 1990), with the base surge reaching Shikine Island situated 13 km from Kozu Island. The pyroclastic cones of Shirashima and Kushigamine created by the Tenjo eruption are distributed northwest and northeast of the Tenjo lava dome, respectively (Taniguchi 1977; Isshiki 1982). Pyroclastic flow deposits of the Tenjo eruption are mainly found at four locations; Nagahama, Sawajiri-wan, and Maehama along the northwest coast of Kozu-shima, and Tako-wan on the east coast (Taniguchi 1977; Togashi 1984). The total mass of pyroclastic matter generated during the Tenjo eruption is estimated at 1.7×10^{12} kg (Ito 1990).

Characteristics of the Tenjo pyroclastic flow deposit

The pyroclastic flow deposit has white-gray in color with a thickness of at least 30 m. The pyroclastic flow deposits can be divided into 5 to 11 flow units. Each flow unit can be subdivided into three subunits based on the differences in lithofacies.

Flow subunit I (lowest unit) shows no grading and comprises of lapilli and volcanic blocks. Its thickness ranges from 30 cm to 10 m and represents the primary part of the pyroclastic flow.

Flow subunit II (middle unit) that exhibits prominent parallel and cross bedding, comprises components as varied as coarse ash and lapilli. Interpreted as a pyroclastic surge deposit, its thickness ranges from a few millimeters to a few centimeters.

Flow subunit III (upper unit) exhibits a prominent mantle bedding comprising of very fine grained material. Construed as a fallout deposit, its thickness is approximately a few millimeters (Fig. 2).
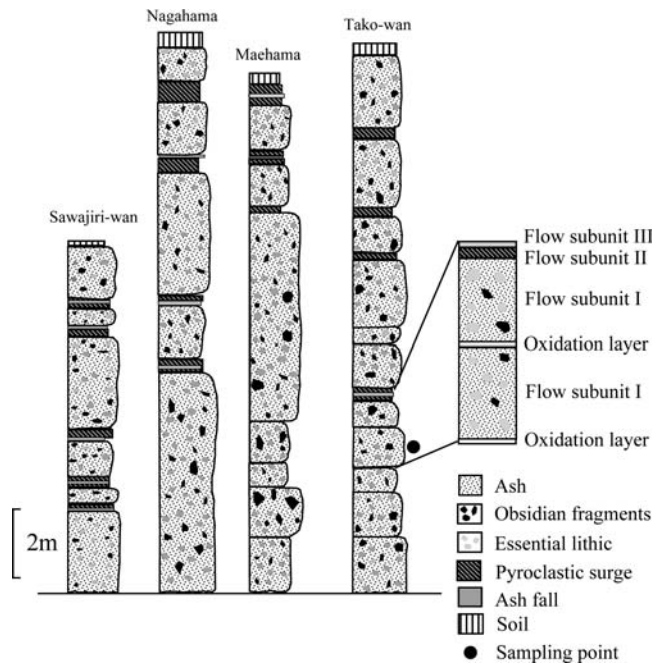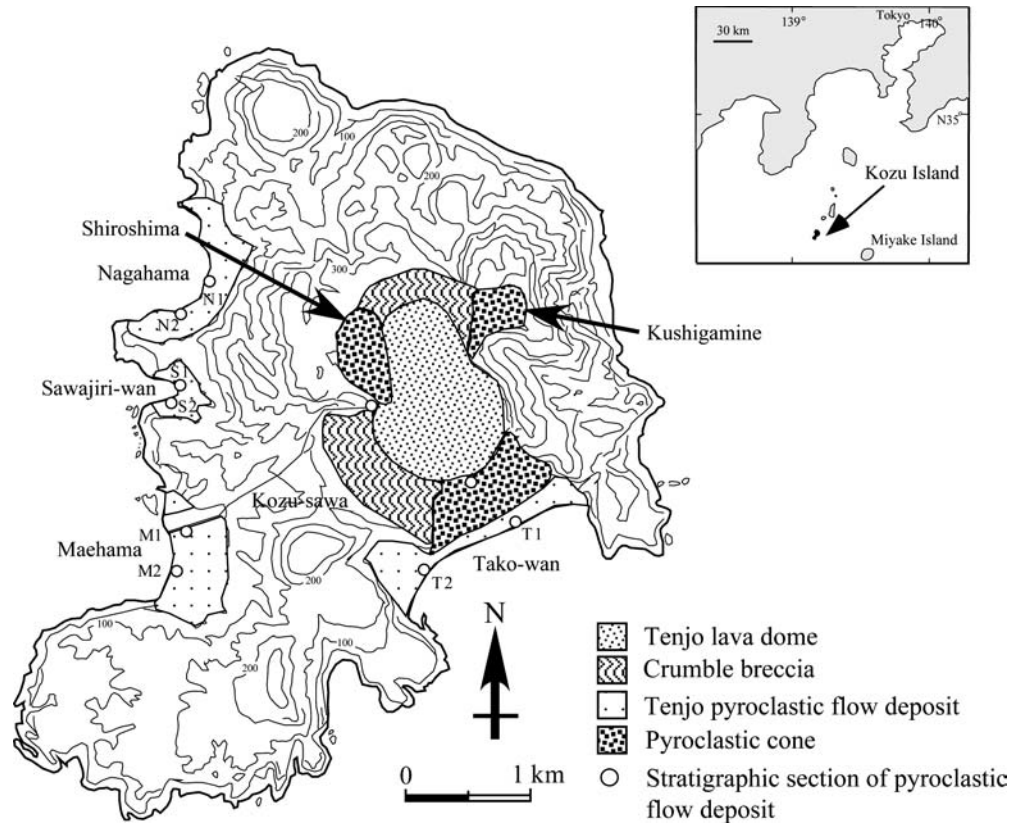
Fig. 2 Stratigraphic columns of the Tenjo pyroclastic flow deposit that represent the outcrops at four locations. The thickness of each pyroclastic flow unit ranges from 30 cm to 10 m

Some flow units contain only flow subunit I while lacking flow subunits II and III. However, we can identify flow boundaries from the presence of oxidized layers, which indicate a time interval between the two flow events

(Fig. 2). A characteristic feature of the primary part of the pyroclastic flow in a flow unit is that it contains both vesicular pumices and obsidian fragments with an approximate maximum diameter of 30 cm. The vesicular pumices and obsidian fragments are sub-rounded and sub-angular in shape, respectively. The obsidian fragments have fractured surfaces. Some flow units in the Tako-wan pyroclastic flow deposit appear to contain pyroclasts of various densities. On the other hand, in the primary part of the pyroclastic flow deposit from Maehama, Sawajiri-wan, and Nagahama, most of the pyroclasts contains few vesicular pumices with a narrow range of bulk densities. Thus, a wide range of bulk densities in a pyroclastic flow deposit can only be observed in the Tako-wan locality. Although the entire sequence of events during the Tenjo eruption have not been clearly understood, the relative thickness of each flow unit of the Tenjo eruption products indicates that the Tenjo pyroclastic flow eruptions were of a small volume (Ito 1990). In this study, we focus on a single eruption of the Tako-wan pyroclastic flow that displays the bulk density variation, and consider neither the entire sequence of eruptive events nor the activity of the pyroclastic eruptions of Tenjo.

Analytical methods

Sample descriptions

The Tako-wan pyroclastic flow deposits (flow subunit I) are characterized by a wide bulk density range of vesicular

pumices in a flow unit, and their lithofacies do not show any grading. Therefore, in this study, we randomly sampled a total of 20 kg of pyroclasts including the matrix ash in a flow unit (flow subunit I) of the Tako-wan pyroclastic flow deposit (T1, Fig. 1). The pyroclastic flow deposit is approximately 1.1 m thick including pyroclasts and obsidian fragments with maximum diameters of 10 and 15 cm, respectively (Fig. 2). All samples selected for analysis were 2–3 cm in size. The dome rock samples were drawn from the summit of the Tenjo lava dome. The dome rocks exhibit few and similar vesicularities suggesting that the bulk densities were not significantly altered during the effusion. For the textural analysis, thin sections with polished surfaces were used.

Bulk density

The bulk density estimation was carried out at Nihon University using a helium pycnometer (Accupyc 1330). First, the dry weights of 159 samples (83 pyroclasts, 76 dome rocks) were measured. Next, the temperature was raised to the melting point of paraffin (more than 60°C). Then, paraffin was introduced into the samples by using a vacuum pump to prevent helium gas from penetrating into the interior of the samples. Finally, the volume of the paraffin-coated pyroclasts was measured. The error in this method is within ± 0.02 cm^3 for 100 cm^3 samples (0.02%). The measurements were carried out twice per sample to verify reproducibility. The standard deviation (1σ) of volume measurement in our samples (<10 cm^3) is approximately $\pm 1.5\%$. Even the porosities were estimated using the helium pycnometer that was used to measure the DRE density of the powdered samples of pyroclasts in the case of Tako-wan. The maximum DRE density (2,490 kg/m^3) was defined as the porosity free density (Average DRE density is 2,430$\pm$50 kg/m^3). Although the density is as accurately estimated by the paraffin method, the same samples cannot be used for textural analysis since the paraffin cannot be extracted from the vesicles.

Textural analysis

For the vesicle textural analyses (vesicularity, vesicle shape, mean bubble size, bubble number density and bubble size distribution (BSD)), 28 samples were used; further, for the crystal (microlite) textural analyses (crystal volume, mean crystal size, crystal number density and crystal size distribution (CSD)), 16 samples were used. The vesicle and crystal textures were determined from binary images obtained from a microscope using reflected light. The digital photographs that were taken were stored in a computer. The outline of each bubble and crystal was then manually traced using application software (Canvas). The number, shape, size, and volume of the bubbles and crystals were measured with the NIH Image Program. The number density was then converted from two dimensions (n_a) to three dimensions (n_v). The bubble number density in three dimensions is calculated by the formula given by Gray (1970):

$$Z = \frac{\pi n_a}{2r} \tag{1}$$

$$n_v = \frac{Z}{1-\phi}, \tag{2}$$

where n_a, r, n_v, and ϕ are the bubble number density per unit area, mean bubble radius in two dimensions, bubble number density per unit volume, and vesicularity, respectively. To measure the microlites, only the area within the groundmass (the bubble-free region) was traced. The CSD Correction method by Higgins (2000, 2002) was used to calculate the microlite number density (area; <300 μm^2) and crystal size distribution. The crystal size distributions were calculated by different stereological methods using BSD determination, because the shape effect of the crystal, unlike in spherical bubbles, hinders the accurate determination of the particle size distribution (Sahagian and Proussevitch 1998). The cut section effect in monodisperse and polydisperse spheres, the cut section effect has been well studied (Saltikov 1958). However, in non-spherical-shaped objects, the intersection probability produces some error. Some studies provide improved methods to account for the cut effect by using the aspect ratio of particles (Sahagian and Proussevitch 1998; Higgins 2000, 2002). Consequently, in the present study, we used the stereological method studied by Higgins (2000, 2002).

Compositional analysis

The mineral and glass compositions were determined at the Department of Earth Science, Kanazawa University, using a JEOL 8800 Electron Probe Micro-Analyzer (EPMA): a focused beam (3–5 μm) with a 15-keV accelerating voltage and 10-nA beam current was used. The loss of NaK-α X-ray intensity during EPMA analysis poses a serious problem in the determination of the chemical compositions of glass samples. An empirical correction method to account for the Na-loss has been developed (Nielsen and Sigurdsson 1981; Devine et al. 1995; Morgan and London 1996). This method involves the monitoring of the decay curves of X-ray intensity and the estimation of the true Na intensity at 0 s. However, the raw Na X-ray counts cannot be obtained from the monitor mode of our EPMA. In this study, we determined the time dependent decay profile from the digital data obtained from a line scan mode using a focused beam (5 μm) without moving the spot under analysis for 20 s (Noguchi et al. 2004). Noguchi et al. (2004) used the glass samples from the Tenjo eruption to evaluate the error in this method. The corrected values of Na and K obtained by the present method are in good agreement (within ± 0.3 wt%) with the chemical compositions determined by the defocused beam mode (30 μm analysis).

H₂O analysis

Bulk H_2O contents were determined by Karl Fischer titration (KFT) and a thermogravimetric and differential thermal analyzer (TDTA). KFT was carried out at ERI, University of Tokyo, while TDTA was performed at the Department of Earth Sciences at Kanazawa University. The KFT method is described by Westrich ([1987]) and Shimano and Koyaguchi ([2001]). The TDTA involves the utilization of the weight difference in discharged water between a powdered sample and a standard sample (anhydrate Al_2O_3) for the analysis. The samples were heated at 150°C for 1 h to evaporate the absorbed water, and at 1,050°C for 1.5 h to verify the amount of water dissolved. The same pyroclast sample was separately measured three times to verify reproducibility. The initial volatile contents in the glass inclusions in the phenocrysts were determined by the EPMA-difference method (Devine et al. [1995]; Morgan and London [1996]) where total volatiles (mostly H_2O) = 100 wt% - the total wt% of measured elements. Devine et al. ([1995]) suggested that this method tends to produce a large error (>0.5 wt%) because of Na-loss and Al and Si grow-in during EPMA of SiO_2-rich glass. However, Morgan and London ([1996]) indicated that the low-energy defocused beam of EPMA ensures a more accurate H_2O estimation when compared with the estimation from the FTIR method for glass containing >1 wt% H_2O. In our samples, the error analysis shows that the corrected value of Na, K, Si, and Al by the decay-curve method is in good agreement (within ±0.3 wt%) with the value obtained by the defocused beam. Although the uncertain error in the EPMA-difference method is large, this method greatly reduces the error. It can therefore be concluded that the corrected value is acceptable for H_2O estimation of initial volatile content.

Results

Bulk density

Figure [3] shows the bulk density of the pyroclasts in the Tako-wan pyroclastic flow deposit and the dome rocks. The bulk densities in a single flow unit of pyroclasts range from 300 to 2,060 kg/m³ (average density 1,330 kg/m³), while the porosities range from 17 to 87% (average porosity 46.5%). Obsidian fragments exhibit high densities that range from 2,320 to 2,420 kg/m³ (porosity ranging from 3 to 7%). Dome rocks exhibit a narrower range of bulk densities when compared with the pyroclasts of Tako-wan (1,420–2,180 kg/m³, average density 1,820 kg/m³), which corresponds to the porosity variation from 14.2 to 42.8% (average porosity 27.0%). Standard deviation (1σ) of the porosities in the Tako-wan pyroclastic flow deposit and the dome rocks are ±21.8 and ±6.7%, respectively. A relatively wide range of densities is observed in the Tako-wan pyroclastic flow deposit.
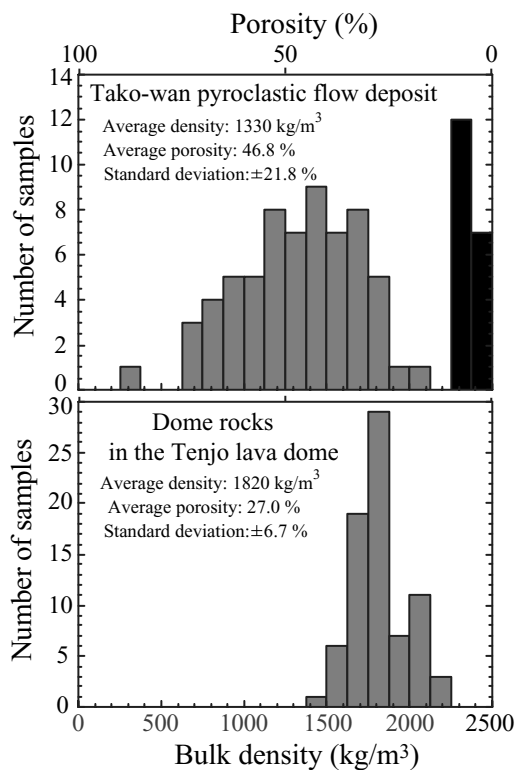

Fig. 3 The bulk density distributions of pyroclasts and obsidian fragments in the Tako-wan pyroclastic flow deposit and in dome rocks. *Gray* and *black* colors indicate pyroclasts and obsidian fragments, respectively. Pyroclasts exhibit a wide range of vesicularities

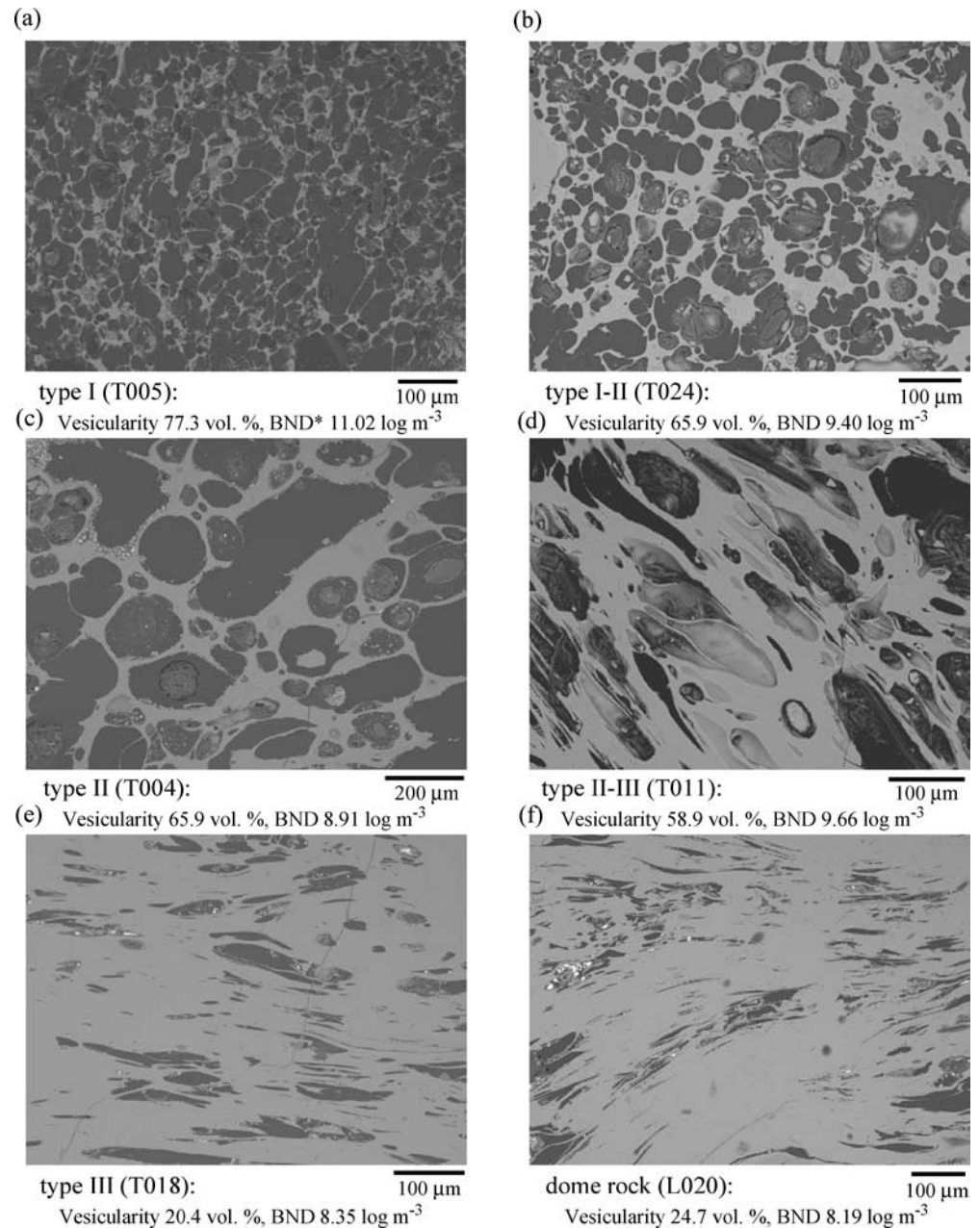Textural analyses

Vesicle texture

The wide density range of pyroclasts in a single flow unit of the Tako-wan pyroclastic flow deposit can be related with the various vesicle textures. We therefore classify the pyroclasts into three types–type I, type II, and type III–based on their vesicle textures (Fig. [4]).

In type I, most bubbles are spherical in shape (aspect ratio 0.58–0.73) and relatively small in size (average radius 8–16 μm). Some bubbles bear coalescence signatures. Large-sized bubbles are not observed. The bubble number densities (10.8–11.7 log m⁻³) and vesicularities (67–77 vol%) are higher than that for the other types of pyroclasts. Type I depicts an exponential law distribution in the bubble size distribution (BSD) curve (Fig. [5]b).

In comparison to type I, most bubbles in type II are larger in size (41–64 μm) and show coalescence (aspect ratio 0.57–0.65). Small-sized bubbles were not observed in the thin section. Although the vesicularity is almost the same (relatively decreasing) as in type I, the bubble number densities (8.9–9.5 log mm⁻³) are lower than that in type I. The BSD shows an exponential distribution.

In type III, the bubbles are extremely deformed (aspect ratio 0.34–0.49). Small-sized spherical bubbles are not observed in the thin section. The bubble number densities (8.2–9.0 log mm⁻³) and vesicularities (16–34 vol%) are

Fig. 4 Scanning electron microscope (SEM) images showing various vesicle textures. **a** Small spherical bubbles with high vesicularity (type I); **b** Coexisting textures of small spherical and coalesced bubbles (type I–II); **c** Coalesced bubbles with a vesicularity similar to that of type I (type II); **d** Elongate bubbles with a low aspect ratio (type II–III); **e** Highly deformed bubbles with low vesicularity (type III); **f** Vesicle textures similar to type III (dome rock)

(a)
type I (T005): 100 μm
Vesicularity 77.3 vol. %, BND* 11.02 log m⁻³

(b)
type I-II (T024): 100 μm
Vesicularity 65.9 vol. %, BND 9.40 log m⁻³

(c)
type II (T004): 200 μm
Vesicularity 65.9 vol. %, BND 8.91 log m⁻³

(d)
type II-III (T011): 100 μm
Vesicularity 58.9 vol. %, BND 9.66 log m⁻³

(e)
type III (T018): 100 μm
Vesicularity 20.4 vol. %, BND 8.35 log m⁻³

(f)
dome rock (L020): 100 μm
Vesicularity 24.7 vol. %, BND 8.19 log m⁻³

smaller than those in type II. The dome rocks exhibit textures similar to type III (Fig. 4, Table 1). Both type III and dome rocks exhibit an exponential distribution in the BSD curve. The peaks of the curves are aligned toward lower number densities as compared to type II.

Figure 5a and b show the results of the textural analyses of the bubbles. Intermediate vesicle textures between types I and II (small spherical and large bubbles, respectively) coexist within a single thin section. The characteristics of vesicle textures between types II and III typically show elongate bubbles with low aspect ratios. However, the intermediate vesicle textures between types I (small spherical bubble) and III (deformed bubble) do not coexist within a single thin section indicating a systematic and continuous change from small spherical bubbles (type I) to coalesced bubbles (type II) through elongated bubbles to highly deformed bubbles (type III). Type I has the highest bubble number density, highest vesicularity and smallest dominant bubble size. Type II has almost the same vesicularity as type I, but the bubble number density is lower than type I due to the coalesced bubbles. Type II–III pyroclasts have a low aspect ratio due to elongate bubbles. Type III has almost the same bubble size as type II (relatively smaller size than type II), but the bubble number density decreases with decreasing vesicularity. There is a positive correlation between bubble number density and vesicularity among these three types (Fig. 5a). For the BSD curves, type I pyroclasts exhibit an exponential law distribution. However, large-sized BSD curves are not linear (shape of a power-law-like distribution). The power law distribution
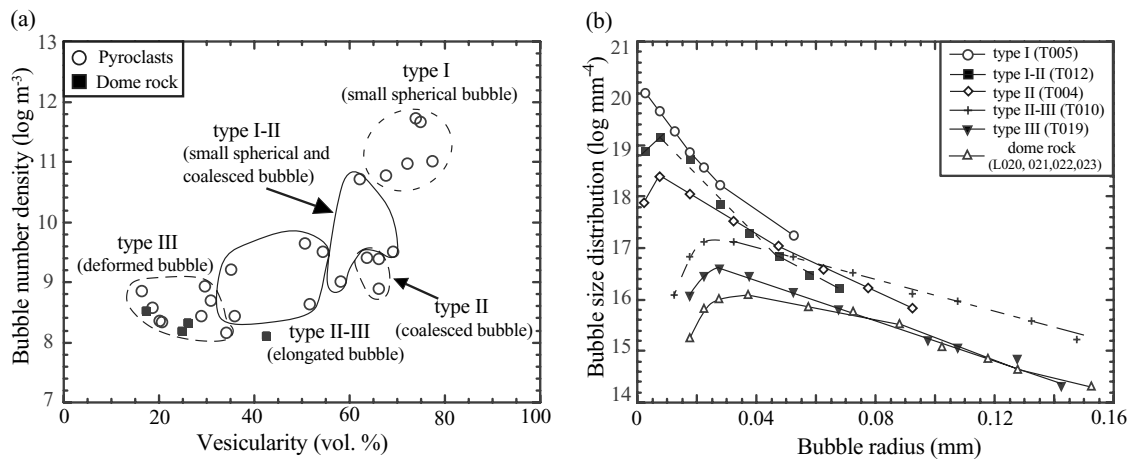
Fig. 5 **a** Graph of bubble number density against vesicularity. The systematic change in vesicle textures from type I to type III correlates well with the decreasing number density and vesicularity. **b** Graph showing the bubble size distribution for three types of pumices and dome rocks. The bubble radius indicates the equivalent circle radius
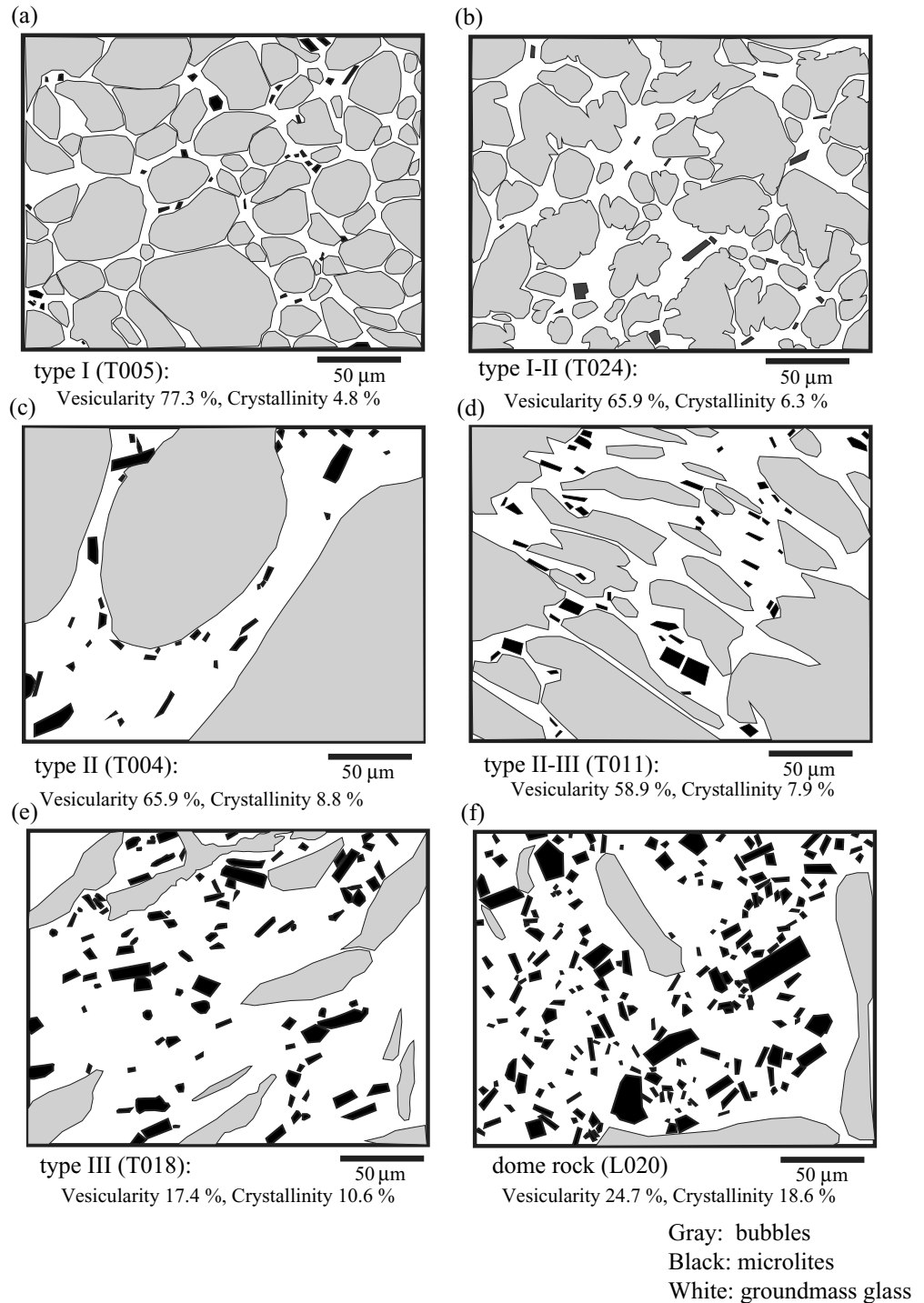
of large-sized in type I pyroclast shifts to exponential distributions (type II). Since the total bubble number density decreases with the absence of small bubbles, the peak of the curves shift to the right side (large size). For type III and dome rocks, the shapes of the BSD curves are exponential distribution, similar to type II, but the peaks of the curves move downward toward lower number density due to low vesicularity.

Table 1 Vesicle textural analysis

Sample	Vesicular type	Vesicularity (vol. %)	Area (mm^2)	Number of bubbles	Aspect ratio	Avg. Bubble radius (mm)	Na (m^{-2})	Nv (log m^{-3})
T005	I	77.3	0.42	360	0.58	0.013	8.E+08	11.02
T007	I	72.1	0.58	566	0.66	0.016	1.E+09	10.98
T025	I	74.8	0.27	670	0.70	0.008	3.E+09	11.67
T026	I	67.5	1.45	916	0.65	0.016	6.E+08	10.79
T027	I	73.7	0.28	804	0.73	0.008	3.E+09	11.74
T024	I–II	65.9	0.41	235	0.58	0.021	3.E+07	9.40
T012	I–II	61.9	1.44	779	0.64	0.016	5.E+08	10.72
T009	I–II	58.0	12.54	527	0.48	0.042	4.E+07	9.03
T015	II	63.4	5.04	335	0.65	0.041	7.E+07	9.41
T004	II	65.9	7.41	244	0.58	0.064	3.E+07	8.91
T003	II	68.9	3.11	404	0.57	0.062	1.E+08	9.52
T016	II–III	54.3	2.46	206	0.38	0.040	8.E+07	9.52
T013	II–III	51.6	9.27	179	0.52	0.069	2.E+07	8.64
T011	II–III	50.6	2.32	242	0.44	0.036	1.E+08	9.66
T010	II–III	35.7	15.79	211	0.33	0.074	1.E+07	8.45
T006	II–III	35.1	3.43	174	0.42	0.048	5.E+07	9.22
T002	III	34.0	5.60	41	0.41	0.076	7.E+06	8.18
T030	III	18.5	15.78	224	0.34	0.057	1.E+07	8.59
T008	III	16.3	14.68	339	0.49	0.049	2.E+07	8.87
T017	III	20.1	6.52	64	0.38	0.066	1.E+07	8.37
T018	III	20.4	15.78	156	0.45	0.070	1.E+07	8.35
T001	III	28.8	6.01	84	0.41	0.078	1.E+07	8.45
T014	III	29.4	6.90	235	0.42	0.060	3.E+07	8.95
T019	III	30.7	15.84	322	0.49	0.062	2.E+07	8.71
L020	Lava	24.7	6.08	52	0.36	0.086	9.E+06	8.19
L021	Lava	42.4	6.26	50	0.48	0.095	8.E+06	8.12
L022	Lava	17.3	6.99	82	0.44	0.054	1.E+07	8.53
L023	Lava	25.9	6.49	70	0.52	0.081	1.E+07	8.32

Fig. 6 Figure showing the representative microlite textures in three types of pumices and lava domes obtained from binary images using reflected light. The microlites are indicated by black color, bubbles by gray color, and groundmass glass by white color. **a** Type I: low crystallinity and small microlites; **b** Type I–II: textures similar to type I, but crystallinities and sizes are relatively large as compared with type I pyroclasts; **c** Type II: microlite crystallinities and sizes larger than type I; **d** Type II–III: microlite crystallinity is similar to type II pyroclast; however, sizes are large; **e** Type III: microlite crystallinities and sizes are the largest among the three pyroclast types; **f** Dome rock: crystallinities and sizes are the largest among all types

(a) type I (T005): Vesicularity 77.3 %, Crystallinity 4.8 %

(b) type I-II (T024): Vesicularity 65.9 %, Crystallinity 6.3 %

(c) type II (T004): Vesicularity 65.9 %, Crystallinity 8.8 %

(d) type II-III (T011): Vesicularity 58.9 %, Crystallinity 7.9 %

(e) type III (T018): Vesicularity 17.4 %, Crystallinity 10.6 %

(f) dome rock (L020): Vesicularity 24.7 %, Crystallinity 18.6 %

Gray: bubbles
Black: microlites
White: groundmass glass

Microlites

Groundmass microlites comprise of plagioclase, alkali feldspar, quartz, small amounts of biotite (fragments of phenocrysts) and Fe-Ti oxides. The average size of feldspar microlites increases from type I (long length 6 µm) to type III (long length 12 µm) (Fig. 6, Tables 2 and 3). The total volume fraction of the microlites also increases from 4.8 to 15.1 vol% (Fig. 6, Table 2) as the pyroclast type changes from type I to type III.

The number density of microlites does not show any significant variation in its value for type I and type III (Fig. 7a, Table 2). The microlite number density of feldspar in groundmass assumes similar values in the range 5.1–5.6 log mm^{-3} regardless of the type of vesicles (Table 3). Figure 7b shows that the CSDs exhibit exponential

Table 2 Microlite textural analysis

Sample	Vesicular type	Vesicularity (vol. %)	Area (mm^2)	Number of microlites	Length (mm)	Width (mm)	Crystallinity (vol. %)	Na (mm^{-2})	Nv (log mm^{-3})
T005	I	77.3	0.104	307	0.0050	0.0023	4.8 (0.8)	2959	5.50
T007	I	72.1	0.055	253	0.0057	0.0022	6.4 (1.5)	4596	5.08
T026	I	67.5	0.080	246	0.0060	0.0024	4.6 (1.4)	3092	5.55
T024	I–II	65.9	0.212	275	0.0091	0.0040	6.3 (2.6)	1296	5.13
T012	I–II	61.9	0.037	181	0.0087	0.0033	9.0 (2.0)	4904	5.38
T009	I–II	58.0	0.359	690	0.0097	0.0040	7.8 (1.5)	1925	5.02
T015	II	63.4	0.168	451	0.0075	0.0032	8.0 (2.7)	2685	5.53
T004	II	65.9	0.072	292	0.0058	0.0024	8.8 (2.5)	4054	5.75
T003	II	68.9	0.068	220	0.0084	0.0034	7.9 (2.7)	3242	5.71
T011	II–III	50.6	0.141	221	0.0107	0.0042	7.9 (2.2)	1566	5.14
T006	II–III	35.1	0.082	207	0.0092	0.0046	7.6 (2.4)	2531	5.32
T001	III	28.8	0.033	124	0.0089	0.0039	10.7 (2.6)	3767	5.66
T017	III	20.1	0.164	321	0.0109	0.0056	10.6 (3.5)	1953	5.20
T018	III	20.4	0.164	309	0.0076	0.0024	15.1 (5.7)	1880	5.32
T030	III	18.5	0.190	600	0.0097	0.0043	13.0 (3.3)	3153	5.31
L020	Lava	24.7	0.024	181	0.0101	0.0040	18.6 (3.1)	7393	5.31

Table 3 Plagioclase microlite textural analysis

Sample	Vesicular type	Area (mm^2)	Number of microlites	Length (mm)	Width (mm)	Na (log mm^{-2})	Nv (log mm^{-3})
T005	I	0.260	445	0.0063	0.0021	1712	5.32
T007	I	0.030	65	0.0056	0.0018	2167	5.35
T026	I	0.080	223	0.0060	0.0024	2803	5.49
T024	I–II	0.212	263	0.0092	0.0040	1240	5.10
T012	I–II	0.050	122	0.0089	0.0025	2440	5.44
T009	I–II	0.359	661	0.0097	0.0040	1844	5.56
T015	II	0.220	337	0.0081	0.0024	1532	5.20
T004	II	0.280	460	0.0079	0.0026	1643	5.06
T003	II	0.070	127	0.0067	0.0021	1814	5.15
T011	II–III	0.141	221	0.0108	0.0042	1566	5.56
T006	II–III	0.100	83	0.0093	0.0033	830	5.30
T001	III	0.033	113	0.0083	0.0036	3433	5.63
T017	III	0.164	214	0.0113	0.0048	1302	5.21
T018	III	0.164	194	0.0117	0.0049	1180	5.05
T030	III	0.190	384	0.0109	0.0039	2021	5.27
L020	Lava	0.024	142	0.0084	0.0036	5800	5.73

distributions, and the slope of the CSD curves gradually decreases from type I to type III.

Compositional analysis

Feldspar and glass composition

The three types of pyroclasts contain small microlites in the range of 6–12 μm (average long length, Tables 2 and 3). Some microlites do not have a sufficiently large cross sectional area for EPMA analysis; therefore, only larger microlites (minor length 10∼15 μm) are used while performing analyses. Since large microlites are not found in type I, a compositional analysis was performed only for types II and III.

Plagioclase phenocrysts commonly exhibit normal compositional zoning from core (An_{23}) to rim (An_{11}). The phenocryst rims (10 μm in length) are often clear. In addition, the compositions of feldspar microlites overlap with phenocryst rims ranging from $Ab_{78}An_{12}Or_{10}$ to $Ab_{48}An_1Or_{51}$ (Fig. 8). These compositional variations from plagioclase to alkali feldspar are continuous and can be observed in all the samples.

Glass compositions of pyroclasts are shown in Table 4 and Fig. 9. The Na_2O and K_2O contents are approximately constant in comparison to the increase in the SiO_2 content in (Fig. 9). According to the different crystallinities among the vesicular types, the microlite crystallinities in type III (4–9 vol% higher than type I–II) result in an increase in SiO_2 content of glass by slightly 0.4–1.1 wt%. However, the standard deviation in the SiO_2 content of glass tends to
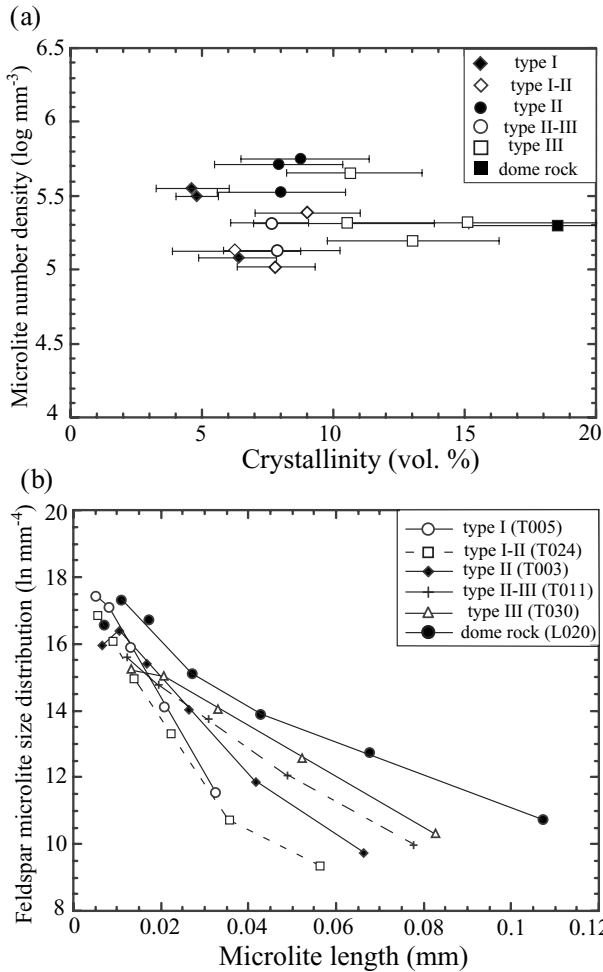
Fig. 7 **a** Graph of the microlite crystal number density against microlite crystallinity. Symbols for type I–II indicate that both types are present, while type II–III shows elongate bubbles. Horizontal bars represent the error analysis of crystallinity. Irrespective of the microlite volume fraction and the type of pyroclasts, the crystal number density is not significantly altered. **b** Graph depicting the microlite CSD of three types of pyroclasts and dome rock sample

be large (from 0.3 to 1.9). Thus, we cannot clearly find the correlation between the SiO_2 content and microlite volume fraction.

H_2O contents

In the pyroclasts from the Tenjo pyroclastic flow deposit, the phenocryst content is less than 10 vol%, while the hydrous mineral biotite content is negligible (0.1–0.3 vol%). That is why the bulk H_2O content in the samples is similar to the H_2O contents in glasses. Table 5 shows the bulk H_2O content and vesicularity of the pyroclastic flow deposit and dome rocks. The bulk H_2O content in all vesicular types is similar (average: 2.6±0.2 wt%, Table 5). However, the H_2O content in the dome blocks is approximately 1.3 wt%. If exsolution of H_2O from the melt proceeded under the equilibrium conditions in the absence of CO_2, the pressure
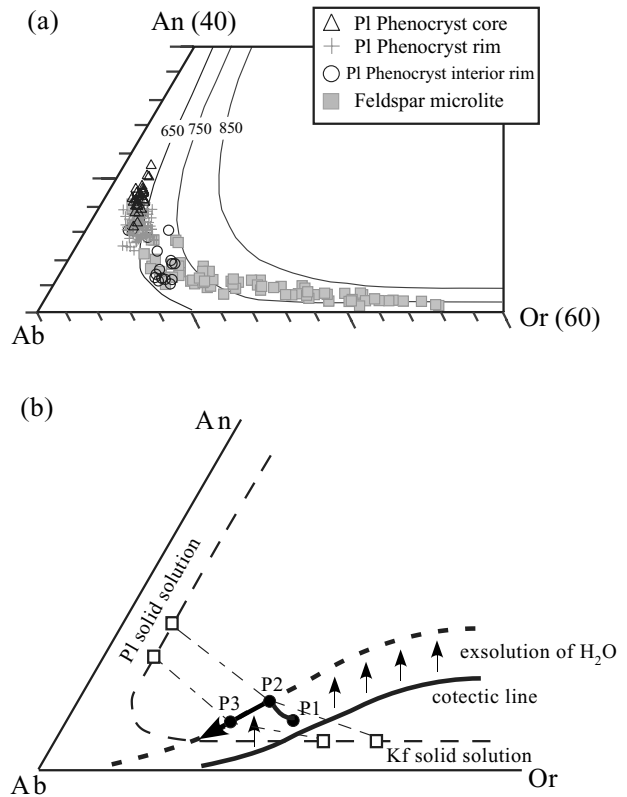

Fig. 8 **a** Ternary diagram depicting the compositions of plagioclase phenocrysts and feldspar microlites. The compositions of phenocryst rims are evolved (Ab-rich) as compared with phenocryst interior rims. The compositional variations from plagioclase to alkali feldspar are continuous, ranging from $Ab_{78}An_{12}Or_{10}$ to $Ab_{48}An_1Or_{51}$ irrespective of the type of pyroclast. **b** A schematic sketch of the crystallization path for feldspar microlites. P1: crystallization of plagioclase phenocryst rims; P2: crystallization of alkali feldspar microlites after exsolution of H_2O; P3: both plagioclase and alkali feldspar solid solutions continuously react with the melt on the cotectic line as they increase in quantity and become Ab-rich. See discussion in text
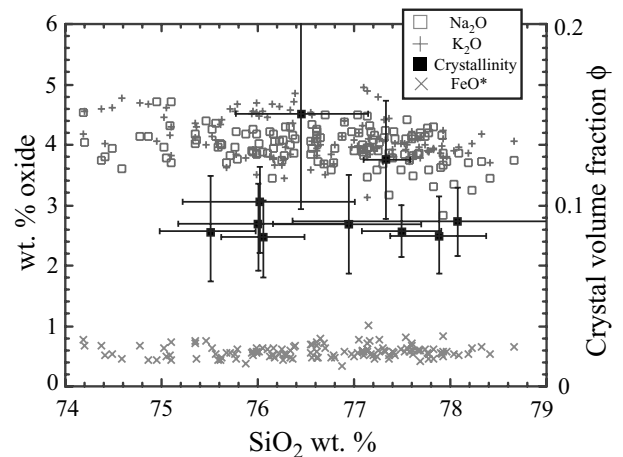

Fig. 9 Glass composition in Na_2O, K_2O, FeO^* and crystal volume fraction in the pyroclastic flow deposit plotted against the SiO_2 content. Na_2O and K_2O contents are similar to the increasing SiO_2 content. *Horizontal bars* represent the standard deviation (1σ) of the SiO_2 content, while *vertical bars* exhibit the error analysis of crystallinity

Table 4 Glass composition in vesicular pumices

	T006	std†	T010	std	T011	std	T014	std	T015	std	T012	std	T009	std	T016	std	T013	std
Vesicularity (vol%)	35.1		35.7		50.6		29.4		63.4		61.9		58.0		54.3		51.6	
Crystallinity (vol%)	7.6		n.d.		7.9		n.d		8.0		9.0		7.8		n.d		n.d	
Sample	T006		T010		T011		T014		T015		T012		T009		T016		T013	
n*	6		6		18		11		6		9		6		18		9	
SiO_2	77.95	0.50	76.57	0.53	76.23	0.43	76.74	0.54	75.57	0.52	78.11	1.87	77.52	0.42	76.60	0.75	78.16	0.52
TiO_2	0.10	0.05	<0.1		<0.1		<0.1		<0.1		<0.1		<0.1		<0.1		<0.1	
Al_2O_3	12.09	0.20	12.11	0.16	11.99	0.13	12.03	0.13	12.40	0.08	11.63	0.49	11.92	0.15	12.14	0.20	12.08	0.11
FeO	0.58	0.06	0.51	0.09	0.56	0.10	0.53	0.08	0.61	0.04	0.53	0.20	0.54	0.06	0.58	0.07	0.55	0.04
MnO	<0.1		<0.1		<0.1		<0.1		<0.1		<0.1		0.11	0.02	<0.1		<0.1	
MgO	<0.5		0.06	0.01	0.05	0.01	0.05	0.02	0.05	0.01	<0.5		0.05		0.06	0.01	0.05	0.05
CaO	0.31	0.04	0.35	0.03	0.32	0.03	0.34	0.03	0.34	0.02	0.28	0.03	0.35	0.03	0.33	0.02	0.36	0.03
Na_2O	3.94	0.17	3.96	0.12	3.98	0.08	3.92	0.10	4.16	0.03	3.19	0.51	3.34	0.14	3.92	0.14	3.43	0.12
K_2O	4.13	0.11	3.89	0.12	4.19	0.10	3.87	0.13	4.30	0.06	3.95	0.48	3.79	0.07	4.08	0.09	3.85	0.10
Total	99.18		97.58		97.45		97.61		97.56		97.85		97.70		97.86		98.64	
Vols. by diff. (wt%)	0.82		2.42		2.55		2.39		2.44		2.15		2.30		2.14		1.36	

	T030	std	T004	std	T003	std	T018	std	T002	std	T001	std	Inclusion glass in Qz T018	std	Inclusion glass in Hb T014	std	Inclusion glass in Hb T011	std
Vesicularity (vol%)	18.5		65.9		68.9		20.4		34.0		28.8							
Crystallinity (vol%)	13.0		8.8		7.9		15.1		n.d		10.7							
Sample	T030		T004		T003		T018		T002		T001		T018		T014		T011	
n	7		4		4		7		4		9		5		5		6	
SiO_2	77.38	0.25	76.02	0.90	76.91	0.78	76.48	0.72	75.33	0.55	76.02	0.90	74.39	0.69	74.08	0.05	73.79	0.09
TiO_2	<0.1		<0.1		<0.1		<0.1		<0.1		<0.1		<0.1		0.10	0.02	<0.1	
Al_2O_3	12.25	0.16	12.01	0.30	11.90	0.32	11.64	0.48	12.21	0.36	12.01	0.30	12.08	0.11	12.17	0.13	11.97	0.07
FeO	0.55	0.06	0.58	0.06	0.73	0.10	0.59	0.08	0.74	0.03	0.58	0.06	0.63	0.06	0.62	0.08	0.75	0.11
MnO	<0.1		<0.1		<0.1		<0.1		<0.1		<0.1		0.11	0.03	<0.1		0.13	0.07
MgO	0.07	0.02	<0.5		0.06	0.01	0.08	0.01	<0.5		<0.5		0.06	0.02	0.08	0.01	0.05	0.03
CaO	0.34	0.04	0.30	0.03	0.30	0.02	0.54	0.09	0.29	0.03	0.30	0.03	0.45	0.04	0.45	0.04	0.34	0.03
Na_2O	4.07	0.41	3.87	0.22	4.23	0.18	3.64	0.36	4.36	0.32	3.87	0.22	3.72	0.05	4.07	0.00	4.08	0.01
K_2O	4.03	0.19	4.62	0.22	4.12	0.19	3.68	0.27	4.12	0.22	4.62	0.22	3.95	0.04	4.63	0.04	4.51	0.19
Total	98.84		97.59		98.40		96.80		97.21		97.59		95.43		96.24		95.69	
Vols. by diff. (wt%)	1.16		2.41		1.60		3.20		2.79		2.41		4.57		3.86		4.31	

*number of measurement, †standard deviation (1σ)

at which the magma was quenched can be estimated by a solubility relationship (Burnham 1975). The estimated quenching pressure is 35±5 MPa for pyroclasts and 8 MPa for dome rocks. Pre-eruptive H_2O contents obtained by a glass inclusion analysis using the EPMA difference method are similar, ranging from 3.9–4.6 wt% (average 4.3±0.4 wt%, Table 4).

Discussion

The timing of vesiculation and magma quenching

The bulk H_2O contents in all vesicular types of pyroclasts indicate that the magma was quenched at a similar pressure of approximately 35±5 MPa. On the other hand, if the glass inclusions preserve the information just before the onset of vesiculation, the pre-eruptive H_2O content in the Tenjo magma is estimated to be approximately 4.3 wt% (110±20 MPa, magma-lithostatic pressure). Hence, the magma must have begun vesiculating at around 110±20 MPa and was probably quenched at 35±5 MPa. However, this value of bulk H_2O might not in fact represent the quench pressure. The bulk H_2O content is controlled by the volatile content of the magma, hydration processes, and the amount of phenocrysts and microlites. Particularly, the hydration processes that occur after deposition pose a serious problem in determining the pre-eruptive volatile content. The key factors in hydration processes are the thickness of the hydration layer, the surface area of particles, and the time duration after deposition. If the hydration efficiency strongly depends on the surface areas of the bubbles (Hammer et al. 1999), the H_2O content of type I pyroclasts must be higher than type II and III pyroclasts. Using the bubble size distribution (Fig. 5b), the surface area of the pyroclasts can be estimated by assuming spherical bubbles of equivalent radii. The surface area calculated in type I pyroclasts is significantly large as compared with type III pyroclasts (different by two orders of magnitude). Irrespective of the vesicular types, similar bulk H_2O contents imply that either the hydration processes do not alter the H_2O con-

tents substantially or it is complete in the entire range of pyroclasts.

The thickness of the hydration layers in the Tenjo eruption can be estimated using the relationship between their thickness of hydration layer (x) and their time duration (t) (Friedman et al. 1966):

$$x^2 = D_{H_2O}t, \tag{3}$$

where D_{H_2O} is the effective hydration diffusivity, which is determined by Taniguchi (1980)as 3.65 $\mu m^2/10^3$ year. The hydration layer of the Tenjo eruption (838 A.D.) as obtained by calculation is apparently in good agreement (within 5 μm) with the observation of the hydration layer on the summit of the dome rock in Tenjo (Taniguchi 1980). Although a hydration layer of approximately 2–3 μm is observed from SEM images in some cracked portions and around the vesicles of the phenocrysts from Tako-wan, most portions in the groundmass glass do not exhibit the hydration layer. This fact suggests that hydration does not affect all the particles. Therefore, we conclude that the hydration does not significantly change the bulk H_2O contents.

Our samples exhibit low phenocryst volumes (less than 10 vol%) and different microlite volumes for each of the three types. The different microlite volumes are likely to have been produced due to the different H_2O contents in pyroclasts. Thus, we must neglect the microlite volume effect in the bulk powder samples. Due to the higher microlite volume in type III (5–10 vol% higher than type I), the H_2O content of type III glass is estimated at approximately 0.2 wt% higher than type I. This effect is statistically negligible. Although the hydration may lead to an overestimate of the bulk H_2O content, we conclude that the vesicular pumices from Tenjo may be quenched at a similar pressure.

Origin of the wide range of vesicularity in pyroclasts from the Tenjo eruption

Although the vesicular pumices are considered to have been quenched at similar pressures, the characteristics of the

Table 5 Bulk H_2O content in vesicular pumices

Sample	Vesicular type	Vesicularity (vol%)	H_2O KFT* (wt%)	H_2O TDTA[†] (wt%)			H_2O avg. Total (TDTA)
T025	I	74.8	2.43	2.28	2.26	2.23	2.3
T026	I	71.9	2.72	2.68	2.69	2.65	2.69
T027	I	73.7	2.36	2.58	2.63	2.52	2.52
T009	I–II	58	2.68	2.49	2.55	2.66	2.59
T015	II	61.3	3.13	2.99	2.91	2.95	2.99
T016	II–III	54.3	2.36	2.52	2.56	2.47	2.47
T011	II–III	58.9	2.26	2.69	2.71	2.45	2.52
T006	II–III	43.6	2.69	2.67	2.63	2.66	2.66
T010	II–III	41.7	2.68	2.27	2.38	2.43	2.44
T014	III	29.4	2.8	2.61	2.64	2.66	2.67
L020	Lava	24.7	1.38	n.d	n.d	n.d	1.38 (KFT)
L022	Lava	17.3	1.33	n.d	n.d	n.d	1.33 (KFT)
L023	Lava	25.9	1.34	n.d	n.d	n.d	1.34 (KFT)

*Karl Fischer titration, [†]Thermogravimetric and differential thermal analyzer

vesicle textures are significantly different. These different vesicle textures imply that different physical processes operated in the conduit.

In type I pyroclasts, most bubbles have spherical shapes and small sizes. BSD curves of type I exhibit an exponential law distribution. However, large-sized BSD curves are not linear (shape of a power-law-like distribution). The power law distribution of bubbles in natural volcanic pumices and in laboratory experiments has been observed in the past (e.g., Klug et al. 2002; Namiki et al. 2003). The power law distribution of bubbles is explained by coalescence or multi-stage nucleation processes (Gaonac'h et al. 1996; Blower et al. 2002). On the other hand, the exponential law distribution of bubbles is often explained by a single nucleation process (e.g., Blower et al. 2002). The characteristics of vesicle textures, including the bubble coalescence signatures in large-sized and isolated small-sized bubbles imply that type I pyroclasts are dominant during the nucleation and coalescence processes.

Most bubbles in type II pyroclasts are large compared to those in type I and type I–II pyroclasts. The BSD curves in types I–II and II exhibit an exponential distribution. However, at smaller sizes the population densities decrease; therefore, a shift from the exponential trend occurs. This decrease observed in BSD and/or CSD curves is often explained by Ostwald ripening (Cashman and Ferry 1988; Higgins 1998; Higgins and Roberge 2003; Larsen et al. 2004). The time scale of Ostwald ripening can be estimated by a formula proposed by Proussevitch et al. (1993);

$$\tau = \frac{r_0^2 P_f S}{4RT D \sigma L},\tag{4}$$

where r_0 is the radius of the smaller bubble; P_f, final experiment pressure; S, melt film thickness; R, universal gas constant; T, temperature; D, diffusivity of water in melt; σ, surface tension of water gas in silicate melts; and L, solubility of water in the melt as a function of pressure. We estimate the Ostwald ripening timescale according to Larsen et al. (2004). The estimated value τ of the modal bubble size (<5 μm) requires 3.6×10^{-4} s for the melt film thickness of 10 μm. This timescale is considerably shortened for a smaller r_0 as τ is proportional to r_0^3 (e.g., Voorhees 1985; Larsen et al. 2004). However, bubbles with large perimeters in type II pyroclasts require a significantly longer time to grow by Ostwald ripening. We believe that the presence of small bubbles around larger ones of type I–II pyroclasts indicates a possibility of the occurrence of Ostwald ripening in the conduit. However, only a small part of the large perimeter of bubbles of type II pyroclasts is generated by Ostwald ripening because the growth time during the ascension of magma is insufficient. As shown in Fig. 4c, the morphological signatures of bubble coalescence reveal on observation that the decrease in bubble number density from type I to type II is caused by the coalescence of small spherical bubbles. Therefore, we believe that the coalescence is probably the dominant coarsening mechanism in BSD.

In type III pyroclasts, the bubbles are highly deformed. Coalesced and small spherical bubbles were absent in the thin section; therefore, nucleation and coalescence do not appear to occur. The decrease in bubble number density, vesicularity, and bubble radius from type II (coalesced bubbles) to type III (highly deformed bubbles) is mainly controlled by the loss of gas from within the bubbles due to degassing (i.e., escape of gas phase out of magma) during magma ascent. Thus, we consider that the characteristics of each type of vesicle texture can be attributed to different physical processes: type I, bubble nucleation and coalescence processes; type II, bubble coalescence and growth processes; type III, bubble collapse and deformation associated with open-system degassing.

In general, the fragmentation of magma is controlled by an abundance of bubbles that are formed due to the increase in the ascent velocity of magma. Typical explosive eruptions, such as Plinian and sub-Plinian, generally produce high vesicular pumices with relatively constant vesicularity as eruption products (e.g., Self and Sparks 1978; Heiken and Wohletz 1985; Houghton and Wilson 1989). Sparks (1978) suggests that the fragmentation of magmas is caused by the bubble expansion that occurs when the vesicularity is around 70%–80%. Proussevitch et al. (1993) also suggests that the bubble coalescence causes instability in the foam and results in the fragmentation of magma. In addition, some studies show that the fragmentation of magma is caused by the overpressure of gas within bubbles when it exceeds the tensile strength of the magma (Mcbirney and Murase 1970, Alidibirov 1994). In our samples, however, pyroclasts exhibit a wide range of vesicularity, and their textures are evidence that the characteristic deformed and collapsed vesicles in type II–III and type III pyroclasts are formed by the open-system degassing. The presence of these deformed and collapsed vesicles implies that the gas overpressure in bubbles was released before the magma fragmentation, suggesting the different types of magma fragmentation mechanisms.

Some other laboratory experiments indicate that the rapid decompression rate of magma produces a high strain rate which acts as a mechanism for fragmentation of magma (Alidibirov and Dingwell 1996, 2000; Spieler et al. 2004). Spieler et al. (2004) dealt with the relationship between porosity and pressure difference (ΔP) to determine the fragmentation threshold. Although the rapid depressurization-induced fragmentation of magma is a possible mechanism for producing the wide range of vesicularity in pyroclasts, these conditions are generally induced due to the collapse events of the lava and the crypt domes at a shallow depth. It is difficult for rapid depressurization induced fragmentation of magma to occur at the quenching pressure of the Tenjo eruption (35 ± 5 MPa). In conclusion, we believe that magma fragmentation in the Tenjo eruption is caused due to the interaction between water and magma.

Based on geological evidence, Ito (1990) has argued that phreatomagmatic explosions occurred during the early stages of the Tenjo eruptions. In our samples, the characteristics of fine particles in pyroclasts show blocky and equant shapes on surface similar to the morphological

features of the base surge deposit in the early stages of the Tenjo eruption (Fig. 10). However, the primary evidences of phreatomagmatic eruption, such as the existence of abundant fine ash particles, chilled margin of particles, and accretionary lapilli, are not found (e.g., Heiken and Wohletz 1985). Some studies conducted thermohydraulic explosions by molten fuel coolant interaction (MFCI) experiments (Zimanowski et al. 1997; Büttner et al. 1999, 2002). They suggested that the abundance of ash grain and their surface textures may be related to the water/magma mass ratios during their interaction. This implies that the phreatomagmatic eruption does not always produce typical surface features such as quench cracks, fine ash coating surfaces, and fine grain size distribution. Büttner et al. (1999) dealt with "dry experiments" (no excess water was present in the erupted system), and their products are similar to our samples suggesting that the explosive water/magma interaction is a possible mechanism for the brittle process of magma fragmentation (Büttner et al. 1999, 2002). The estimated values of the H_2O contents in our samples are constant (2.6 ± 0.2 wt%) irrespective of the vesicularities implying that the magma was quenched at similar pressure. We conclude that the different vesicularities in our samples are probably due to the differences in the degrees of degassing.

Compositional changes of feldspar microlites

The compositional variations in plagioclase phenocrysts from their cores to their rims commonly exhibit a normal compositional zoning, while feldspar microlites show a different compositional trend (Fig. 8a).

Microlite crystallization of alkali feldspar requires a crystallization path from plagioclase + liquid (Pl + L) through the two feldspar + liquid curves (Pl + Kf + L) to alkali feldspar + liquid (Kf + L) (Nekvasil 1990; Nekvasil and Lindsley 1990). While the ascending magma behaves as a uniform isothermal system, the crystallization of alkali feldspar may be due to the exsolution of H_2O, resulting in an increase in the liquidus temperature rather than simple cooling (Nekvasil 1992; Hammer et al. 2000). Although the compositional variation as a function of microlite sizes could not be observed, the compositional trend of similar crystal sizes may have resulted from the following processes.

Crystallization of plagioclase rims initially occurred in the Pl + L field (Fig. 8b–P1). As the exsolution of H_2O raises the two feldspar + liquid curves toward those of anorthite (Hammer et al. 2000), the crystallization path may join the cotectic curve, thereby initiating the crystallization of alkali feldspar (Fig. 8b–P2). Subsequently, the crystallization path follows the cotectic line (broken line in Fig. 8b). At the latest stage of crystallization, both plagioclase and alkali feldspar solid solutions continuously react with the melt on the cotectic line as they increase in quantity and transform into Ab-rich compositions (Fig. 8b–P3). This model accounts for the compositional variation of feldspar microlites shown in Fig. 8a.
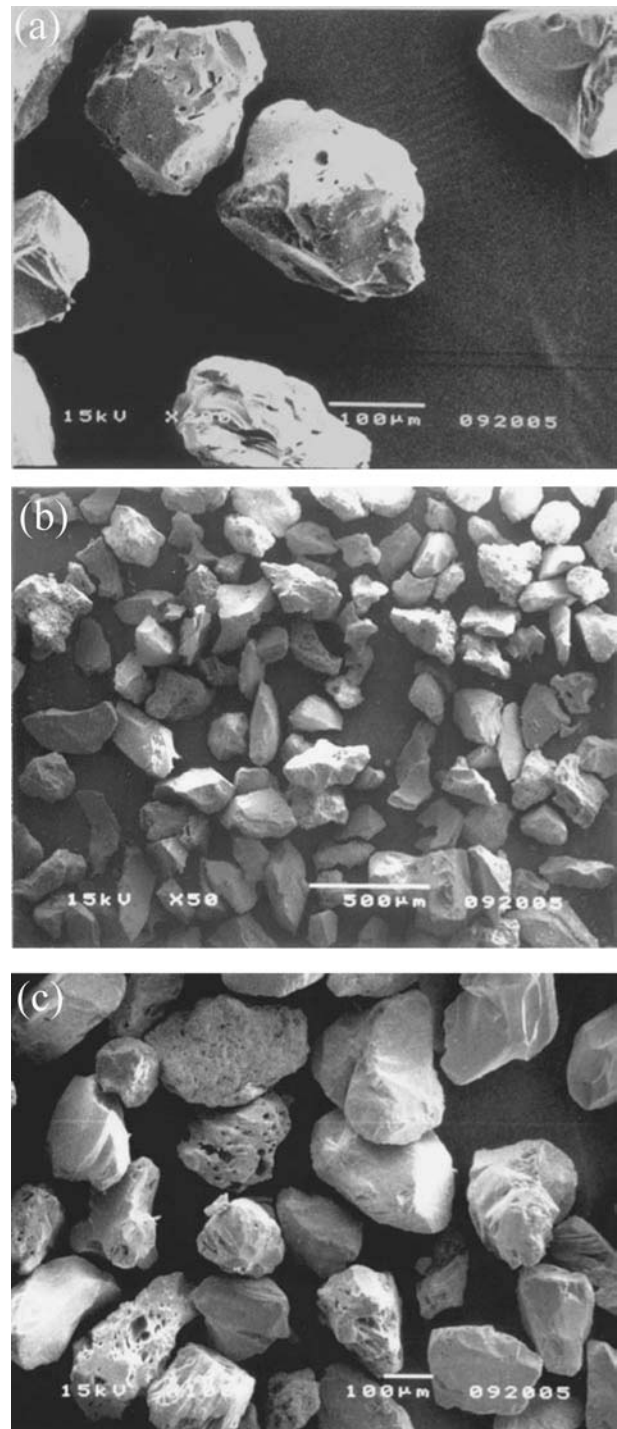

Fig. 10 SEM images of glass particles showing the surface features of the Tako-wan pyroclastic flow deposit and base surge deposit in the early stages of the Tenjo eruption. **a** Fine particles of the Tako-wan pyroclastic flow deposit. The upper left portion of the particle is angular in shape and has stepped surfaces with etches on the surface. **b** Representative fine particles of the Tako-wan pyroclastic flow deposit showing blocky and angular shapes along with flattened surface; **c** Photographs showing the fine particles of the base surge deposit during the early stages of the Tenjo eruption. Most of the particles are blocky-equant shaped similar to those of the Tako-wan pyroclastic flow deposit
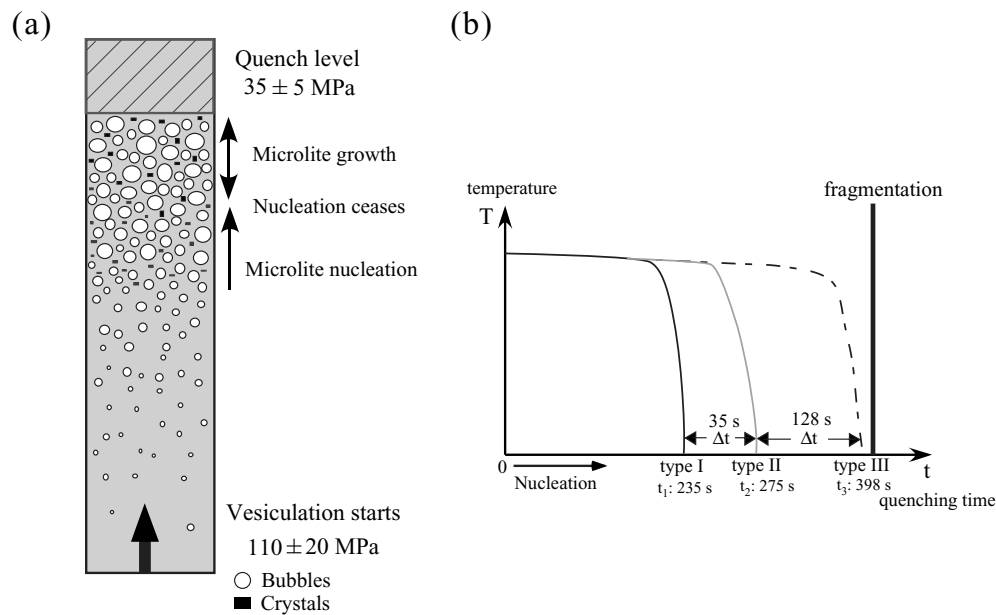
Fig. 11 a Schematic sketch of vesiculation and crystallization in the conduit during the Tenjo eruption. The magma begins to vesiculate at around 110 MPa, and is quenched at 35±5 MPa. Microlite nucleation occurred simultaneously at a particular decompression rate and pressure (H_2O exsolution). **b** Schematic graph illustrating the process from crystal nucleation to quenching as a function of time. The difference in the crystal growth time for type I–II and type II–III can be estimated from the different crystal sizes, provided that the crystal growth rate is constant. If microlite nucleation simultaneously occurs at the vesiculation level, the time scale from vesiculation to quenching can be calculated by the average crystal size and maximum crystal growth rate; type I: 235 s, type II: 270 s and type III: 398 s. Furthermore, the ascent velocity also can be calculated as 7.5, 11, and 13 m/s for type I, II, and III pyroclasts, respectively

On the other hand, the glass compositions in SiO_2 content of pyroclasts are not correlated with increasing microlite crystallinity (Fig. 9). For the mass balance calculation, microlite crystallinities in type III (4–9 vol% higher than type I–II) increases the SiO_2 content in the glass composition by approximately 0.4–1.1 wt% if we suppose that the all microlites consist of feldspar microlite. However, actual eruption products contain plagioclase, alkali feldspar, and quartz microlite. Hence, increase the SiO_2 content in the glass is expected to be low because the crystallization of quartz decreases the SiO_2 content.

The glass compositions in Na_2O and K_2O of pyroclasts are nearly constant for the variation in SiO_2 content. Na_2O and K_2O contents are also determined by the crystallization of plagioclase (Na-rich, K-poor), alkali feldspar (Na-poor, K-rich), and quartz microlite (both increase). According to the mass balance calculation, Na_2O and K_2O contents in the glass is not significantly changed within 0.15%. This fact suggests that microlite crystallization do not largely change the glass compositions.

Crystal nucleation and growth processes

Our samples show that the number density of microlites is almost the same for all three types. However, the total volume fraction of microlites in them is variable. These facts imply that the crystal nucleation must have occurred at a certain depth under a certain decompression rate (Fig. 11a) followed by different growth processes.

As the crystal number density is determined by the effective cooling rate (dT/dt, Toramaru 1991; Toramaru 2001), similar values of crystal number density imply that the changing rates of the pressure and temperature (i.e., exsolution rate of H_2O where effective ΔT is related to ΔP) were similar for different types of pyroclasts. It is likely that the magma system behaved as a uniform isothermal system during magma ascent in the conduit, and the effect of cooling by thermal conduction was negligible during conduit flow (Appendix A). Hence, the crystal growth processes are controlled by the effective ΔT induced only by decompression and water-exsolution from the melt. Some experiments on crystal growth kinetics (Hammer and Rutherford 2002; Couch et al. 2003b) show that the crystal growth rate does not significantly change (one order of magnitude) with the effective ΔT (Hammer and Rutherford 2002, Fig. 13; Couch et al. 2003b, Fig. 12a). Assuming that the crystal growth rate is constant, the crystal growth time equals the magma residence time. Since crystal sizes are determined primarily by the maximum crystal growth rate, we use the maximum crystal growth rate suggested by Hammer and Rutherford (2002) as 8.0×10^{-6} mm/s. The differences in growth times for types I and II and types II and III obtained from the average size of feldspar microlites can be estimated as 43 and 132 s, respectively (Fig. 11b). If crystal nucleation had occurred at the same pressure (lithostatic pressure) after the onset of vesiculation (about 110 MPa), the residence time between the onset of vesiculation and quench is calculated as 235, 270, and 398 s for types I, II, and III, respectively. The magma ascent rate can also be
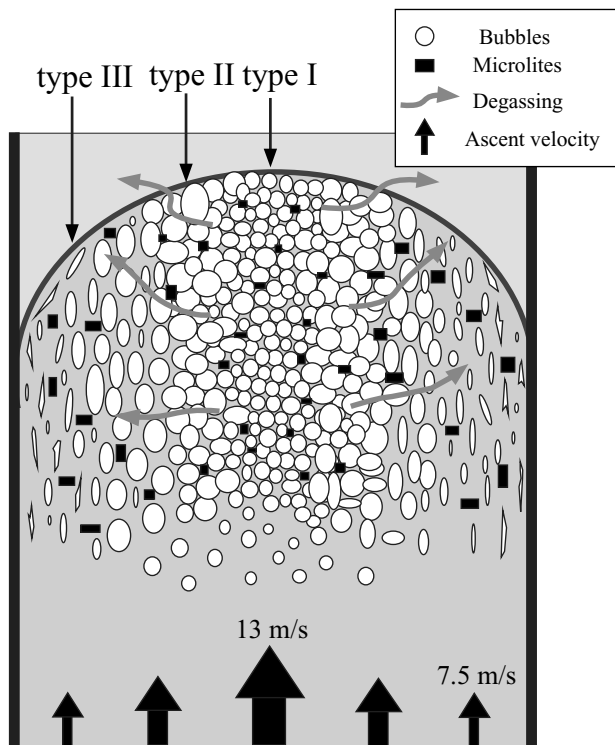
Fig. 12 Schematic model showing the magma ascent process in the conduit during the Tenjo eruption. By assuming a laminar flow such as Poiseuille-type flow, the vesicle and microlite textures can be satisfactorily explained. If type I, II, and III magmas are sequentially distributed from the inner to the outer part of the conduit, the difference in the ascent velocity and shearing motion across the conduit result in different growth times of crystals and the deformation and coalescence of bubbles. The degassing behavior observed in type II and III indicates that the degassing is directed towards the conduit wall

estimated as 13, 11, and 7.5 m/s for types I, II, and III, respectively. Thus, different ascent velocities can be expected during flow through a conduit.

Laminar flow model

Since a laminar flow such as Poiseuille flow displays a velocity gradient across the conduit, a difference in the travel time (i.e., growth time) from nucleation to quenching of crystals is expected. In such a case, the crystal growth time from nucleation to quench in the inner part of the conduit may be shorter because of a higher ascent velocity. If type I magma is located in the central part of the conduit, the crystals become smaller and also preserve small spherical bubbles because of a small macroscopic shear. However, at the margin of the conduit where the ascent velocity is lower, the crystal growth time is long and the shear motion cannot be neglected. When type III magma is distributed along the margin of the conduit, the crystals become larger because of a larger growth time, and the bubbles might coalesce and deform due to a larger shear. If pyroclasts with vesicle textures of types I, II, and III are sequentially distributed from the inner to the outer part of the conduit,

the textural observations can be satisfactorily explained (Fig. 12). This velocity profile in the conduit has been reported (e.g., Castro and Mercer 2004) in other examples, and the large shear-induced fragmentation near the conduit margin generates the intermittent permeable fracture networks that result in the open-system degassing (Stasiuk et al. 1996; Polacci et al. 2001; Gonnermann and Manga 2003). In our samples, the systematic change from type II to type III pyroclasts implies that the efficiency of degassing is possibly a function of the distance from the conduit wall.

Conclusions

We carried out the textural and compositional analyses of pyroclasts from the Tenjo eruption that occurred on Kozu Island. The textural evidence, along with the kinetics of crystallization provides the constraints on the fluid mechanical behavior of magma.

The pyroclasts in a flow unit show a wide variety of vesicle textures and can be divided into three different types that preserve different physical processes: type I, vesiculation and bubble coalescence; type II, bubble coalescence and growth; type III, large deformation by shear stress at the conduit margin as well as the escape of gas (degassing).

In microlite textures, a correlation between vesicular type and crystal number density is not observed; however, this is not the case for that between microlite volume fraction and vesicular type. This implies that the observed changes in microlite textures in the three types are due to changes in the size of each microlite (growth processes) rather than changes in the number density (nucleation processes). Similar number densities indicate the simultaneous occurrence of nucleation under a given decompression (H_2O exsolution) rate. According to the observed H_2O content, magma began to vesiculate at 110 ± 20 MPa and was quenched at a similar depth (35 ± 5 MPa). Although the distance along the conduit during nucleation and quenching are equal, the different crystal sizes of vesicle textures are due to the different growth times arising from the different ascent velocities, assuming a constant crystal growth rate. Laminar flows such as Poiseuille flow can successfully explain this textural observation. Furthermore, the degassing behavior can be considered to be a function of the distance from the conduit wall.
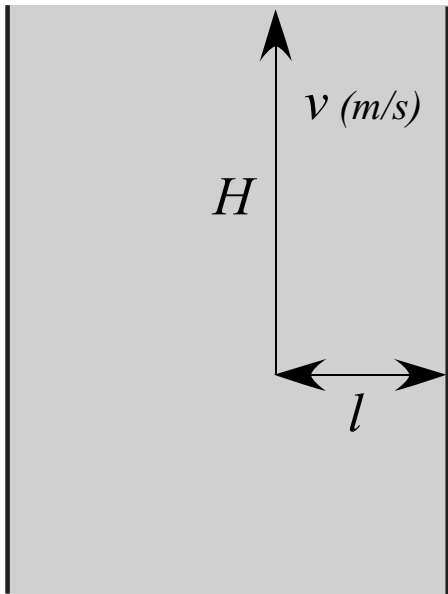
Fig. A1 Photograph representing the schematic images of the relationship between the ascent timescale of magma and the thermal diffusion time scale

Appendix A

Crystal growth induced by cooling at the conduit wall

The crystal growth induced by cooling at the conduit wall may produce varying degrees of crystallization processes. The cooling rate of magma is a function of the distance from the conduit wall, assuming a simple one-dimensional conductive cooling without vertical flow. In such a simple case, the solution for the thermal conduction equation is controlled by a dimensionless quantity $\kappa \sim tx^2$, where κ is the thermal diffusivity, t is time, and x is the distance from the conduit wall (e.g., Carslaw and Jaeger 1959). Here, we consider the relationship between the ascent timescale of magma and the thermal diffusion time scale (Fig. A1); the characteristic time for the ascending magma along the conduit (t_{flow}) is represented as a function of the vertical distance H and the ascent velocity v:

$$t_{\mathrm{flow}} \sim \frac{H}{v}. \tag{A.1}$$

In general, the ascent velocity during typical explosive eruptions is expected to be high, at least 1 m/s. When we assume that the ascent velocity v is 1 m/s and the vertical distance H is 1 km along the conduit, the calculated ascent time t_{flow} is 1.0×10^3 s. On the other hand, during this ascent of magma, the propagation distance of conductive cooling l from the conduit wall can be represented as a function of magma ascent time and thermal diffusivity:

$$l_{\mathrm{th}} \sim \sqrt{\kappa t_{\mathrm{flow}}}. \tag{A.2}$$

After obtaining the heat capacity, melt density, and specific heat proposed by Murase and Mcbirney (1973) and Richet and Bottinga (1986), the thermal diffusivity κ is calculated as 5.5×10^{-7} m^2/s. Thus, the distance of the conductive cooling l is approximately 0.02 m while the magma traverses a vertical distance of 1 km. This implies that the conductive cooling may influence a negligible spatial scale from the conduit wall. Therefore, we believe that crystal growth induced by the cooling at the conduit wall does not play a significant role in the microlite growth process that results in different microlite sizes in various vesicular types.

References

Alidibirov MA (1994) A model for viscous magma fragmentation during volcanic blasts. Bull Volcanol 56:459–465

Alidibirov M, Dingwell DB (1996) Magma fragmentation by rapid decompression. Nature 380:126–148

Alidibirov M, Dingwell DB (2000) Three fragmentation mechanisms for highly viscous magma under rapid decompression. J Volcanol Geotherm Res 100:413–421

Blower JD, Keating JP, Mader HM, Phillips JC (2002) The evolution of bubble size distributions in volcanic eruptions. J Volcanol Geotherm Res 120:1–23

Blundy J, Cashman KV (2001) Ascent-driven crystallization of dacite magmas at Mount St. Helens, 1980–1986. Contrib Mineral Petrol 140:631–650

Burnham CW (1975) Water and magmas: a mixing model. Geochim Cosmochim Acta 39:1077–1084

Büttner R, Dellino P, Zimanowski B (1999) Identifying magma-water interaction from the surface features of ash particles. Nature 401:688–690

Büttner R, Dellino P, Volpe LL, Lorenz V, Zimanowski B (2002) Thermohydraulic explosions in phreatomagmatic eruptions as evidenced by the comparison between pyroclasts and products from Molten Fuel Coolant Interaction experiments. J Geophys Res 107: doi:10.1029/2001JB000511

Carslaw and Jaeger (1959) Conduction of heat in solids. Oxford University Press, Oxford, pp 1–510

Cashman KV, Ferry JM (1988) Crystal size distribution (CSD) in rocks and the kinetics and dynamics of crystallization, III, Metamorphic crystallization. Contrib Mineral Petrol 99:401–415

Cashman KV, Marsh BD (1988) Crystal size distribution (CSD) in rocks and the kinetics and dynamics of crystallization, II, Makaopuhi lava lake. Contrib Mineral Petrol 99:292–305

Castro JM, Mercer C (2004) Microlite textures and volatile contents of obsidian from Inyo volcanic chain, California. Geophys Res Lett 31: doi:10.1029/2004GL020489

Couch S, Harford CL, Sparks RSJ, Carroll MR (2003a) Experimental constraints on the conditions of formation of highly calcic plagioclase microlites at the Soufriere Hills volcano, Montserrat. J Petrol 44: 1455–1475

Couch S, Sparks RSJ, Carroll MR (2003b) The kinetics of degassing-induced crystallization at Soufriere Hills volcano, Montserrat. J Petrol 44:1477–1502

Devine JD, Gardner JE, Brack HP, Layne GD, Rutherford MJ (1995) Comparison of microanalytical methods for estimating H$_2$O contents of silicic volcanic glasses. Am Mineral 80:319–328

Friedman II, Smith RL, Long WD (1966) Hydration of natural glass and formation of perlite. Geol Soc Am Bull 77:323–327

Gaonac'h H, Stix J, Lovejoy S (1996) Scaling effects on vesicle shape, size and heterogeneity of lavas from Mount Etna. J Volcanol Geotherm Res 74:131–153

Geschwind CH, Rutherford MJ (1995) Crystallization of microlites during magma ascent: the fluid mechanics of 1980–1986 eruptions at Mount St. Helens. Bull Volcanol 57:356–370

Gonnermann HM, Manga M (2003) Explosive volcanism may not be an inevitable consequence of magma fragmentation. Nature 426:432–435

Gray NH (1970) Crystal growth and nucleation in two large diabase dikes. Can J Earth Sci 7:366–375

Hammer JE, Cashman KV, Hoblitt RP (1999) Degassing and microlite crystallization during pre-climactic events of the 1991 eruption of Mt. Pinatubo, Philippines. Bull Volcanol 60:355–380

Hammer JE, Cashman KV, Voight B (2000) Magmatic processes revealed by textural and compositional trends in Merapi dome lavas. J Volcanol Geotherm Res 100:165–192

Hammer JE, Rutherford MJ (2002) An experimental study of the kinetics of decompression-induced crystallization in silicic melt. J Geophys Res 107: doi:10.1029/2001JB000281.

Heiken G, Wohletz K (1985) Volcanic ash. University of California Press, pp 1–246

Higgins MD (1998) Origin of anorthosite by textural coarsening: quantitative measurements of a natural sequence of textural development. J Petrol 39:1307–1325

Higgins MD (2000) Measurement of crystal size distributions. Am Mineral 85:1105–1116

Higgins MD (2002) Closure in crystal size distributions (CSD), verification of CSD calculations, and the significance of CSD fans. Am Mineral 87:171–175

Higgins MD and Roberge J (2003) Crystal size distribution (CSD) of plagioclase and amphibole from Soufriere Hills volcano, Montserrat: evidence for dynamic crystallization/ textural coarsening cycles. J Petrol 44:1401–1411

Houghton BF, Wilson CJN (1989) A vesicularity index for pyroclastic deposits. Bull Volcanol 51:451–462

Isshiki N (1982) Geology of the Kozushima district (1:50000 map). Geol Surv Jpn, pp. 75

Ito J (1990) Factor analysis of disaster at Niijima and Kozu-shima, Izu (in Japanese). Chikyu Monthly 21:417–423.

Klug C, Cashman KV (1994) Vesiculation of May 18, 1980, Mount St. Helens magma. Geology 22:468–472

Klug C, Cashman KV, Bacon CR (2002) Structure and physical characteristics of pumice from the climactic eruption of Mount Mazama (Crater Lake), Oregon. Bull Volcanol 64:486–501

Larsen JF, Denis MH, Gardner JE (2004) Experimental study of bubble coalescence in rhyolitic and phonolitic melts. Geochim Cosmochim Acta 68:333–344

Marsh BD (1988) Crystal size distribution (CSD) in rocks and the kinetics and dynamics of crystallization 1. Theory. Contrib Mineral Petrol 99:277–291

Mcbirney AR, Murase T (1970) Factors governing the formation of pyroclastic rocks. Bull Volcanol 64:486–501

Melnik O, Sparks RSJ (1999) Nonlinear dynamics of lava dome extrusion. Nature 402:37–41

Morgan GB, London D (1996) Optimizing the electron microprobe analysis of hydrous alkali aluminosilicate glasses. Am Mineral 81:1176–1185

Murase T, Mcbirney AR (1973) Properties of some common igneous rocks and their melts at high temperatures. Geol Soc Am Bull 84:3563–3592

Nakada S, Motomura Y (1999) Petrology of the 1991–1995 eruption at Unzen: effusion pulsation and groundmass crystallization. J Volcanol Geotherm Res 89:173–196

Namiki A, Hatakeyama, Toramaru, Kurita KA, Sumita I (2003) Bubble size distributions in a convecting layer. Geophys Res Lett 30: doi:10.1029/2003GL017156

Nekvasil H (1990) Reaction relations in the granite system: implications for trachytic and syenitic magmas. Am Mineral 75:560–571

Nekvasil H, Lindsley DH (1990) Termination of the 2 feldspar + liquid curve in the system Ab-Or-An-H_2O at low H_2O contents. Am Mineral 75:1071–1079

Nekvasil H (1992) Ternary feldspar crystallization in high-temperature felsic magmas. Am Mineral 77:592–604

Nielsen CH, Sigurdsson H (1981) Quantitative methods of electron microprobe analysis of sodium in natural and synthetic glasses. Am Mineral 66:547–552

Noguchi S, Morishita T, Toramaru A (2004) Corrections for Na-loss on micro-analysis of glasses by electron probe X-ray micro analyzer (in Japanese with English abstract). J Mineral Petrol Econ Geol 33:85–95

Polacci M, Papale P, Rosi M (2001) Textural heterogeneities in pumices from the climactic eruption of Mount Pinatubo, 15 June 1991, and implications for magma ascent dynamics. Bull Volcanol 63:83–97

Proussevitch AA, Sahagian DL, Kutolin VA (1993) Stability of forms in silicate melts. J Volcanol Geotherm Res 59:161–178

Richet P, Bottinga Y (1986) Thermochemical properties of silicate glasses and liquids; a review. Rev Geophys 24:1–25

Rutherford MJ, Hill PM (1993) Magma ascent rates from amphibole breakdown: an experimental study applied to the 1980–1986 Mount St. Helens eruptions. J Geophys Res 98:19667–19685

Sahagian DL, Proussevitch AA (1998) 3D particle size distribution from 2D observations: Stereology for natural applications. J Volcanol Geotherm Res 84:173–196

Saltikov SA (1958) Stereometric metallography, 2nd edn. Metallurgizdat, Moscow, pp 1–446

Self S, Sparks RSJ (1978) Characteristics of widespread pyroclastic deposits formed by the interaction of silicic magma and water. Bull Volcanol 41:196–212

Shimano T, Koyaguchi T (2001) Eruption styles and degassing process of ascending magma of the 1813 eruption of Suwanose-jima volcano, southwest Japan (in Japanese with English abstract). Bull Volcanol Soc Japan 46:53–70

Sparks RJS (1978) The dynamics of bubble formation and growth in magmas, a review and analysis. J Volcanol Geotherm Res 3:1–37

Spieler O, Dingwell DB, Alidibirov M (2004) Magma fragmentation speed: an experimental determination. J Volcanol Geotherm Res 129:109–123

Stasiuk MV, Barclay J, Carroll MR, Jaupart C, Ratté, Sparks RSJ, Tait SR (1996) Degassing during magma ascent in the Mule Creek vent (USA). Bull Volcanol 58:117–130

Suga K, Kobayashi K, Kanemaki M, Miyahara T, Endo K (1992) Pyroclastic deposits in southern part of Kozushima (in Japanese with English abstract). Bull Volcanol Soc Jpn 37:71–83

Taniguchi H (1977) Volcanic geology of Kozu-shima, Japan (in Japanese with English abstract). Bull Volcanol Soc Jpn 22:133–147.

Taniguchi H (1980) Some volcano-geological significances of the hydration layer observed in the glassy groundmass of Kozu-shima rhyolite (in Japanese with English abstract). Bull Volcanol Soc Jpn 25:217–229

Togashi S (1984) ^{14}C ages pf charcoal from pyroclastics of Tenjosan volcano, Kozushima, the Izu Islands, Japan (in Japanese with English abstract). Bull Volcanol Soc Jpn 29:277–283

Toramaru A (1990) Measurement of bubble size distributions in vesiculated rocks with implications for quantitative estimation of eruption parameters. J Volcanol Geotherm Res 43:71–90

Toramaru A (1991) Model of nucleation and growth of crystals in cooling magmas. Contrib Mineral Petrol 108:106–117.

Toramaru A (2001) A numerical experiment of crystallization for a binary eutectic system with application to igneous textures. J Geophys Res 106:4037–4060

Tsuya H (1929) Volcanoes of Kozu-shima. Bull Earthquake Res Inst 7:269–334

Voorhees PW (1985) The theory of Ostwald ripening. J Stat Phys 38:231–252

Westrich HR (1987) Determination of water in volcanic glasses by Karl Fischer titration. Chem Geol 63:335–340

Wylie JJ, Voight B, Whitehead JA (1999) Instability of magma flow form volatile-dependent viscosity. Science 285:1883–1885

Zimanowski B, Büttner R, Lorenz V (1997) Premixing of magma and water in MFCI experiments. Bull Volcanol 58:491–495